

MPSN: Motion-aware Pseudo-Siamese Network for Indoor Video Head Detection in Buildings

Kailai Sun^{a,1}, Xiaoteng Ma^{a,1}, Peng Liu^{a,1} and Qianchuan Zhao^{a,*}

^aCenter for Intelligent and Networked Systems, Department of Automation, BNRist, Tsinghua University, Beijing, 100084, China

ARTICLE INFO

Keywords:

Indoor video head detection
Building occupancy detection
Motion estimation
Deep features aggregation
Adversarial attack

ABSTRACT

Indoor video head detection is an essential component of building occupancy detection. While deep learning models have achieved remarkable progress in general object detection, their performance is limited in complex indoor scenes. Indoor surveillance videos often contain cluttered background objects, among which heads have small scales and diverse poses. In this paper, we propose Motion-aware Pseudo-Siamese Network (MPSN), an end-to-end approach that leverages head motion information to guide deep learning models to extract effective head features in indoor scenarios. By taking the pixel-wise difference between adjacent frames as the auxiliary input, MPSN effectively enhances human head motion information and removes irrelevant background objects. Its performance is compared with that of existing methods. Compared with existing methods, MPSN achieves superior performance on two indoor video datasets. It successfully suppresses static background objects and highlights the moving instances, especially human heads in indoor videos. Different methods to capture head motion also were compared. MPSN demonstrates simplicity and flexibility compared to other methods. We validate its robustness through adversarial experiments with a mathematical solution of small perturbations for robust model selection. To confirm its potential in building control systems, we apply MPSN to occupancy counting. The code is available at <https://github.com/pl-share/MPSN>.

1. INTRODUCTION

The human dimension information plays a significant role in efficient building energy-saving and comfortable indoor environments (Rueda, Agbossou, Cardenas, Henao and Kelouwani, 2020; Sun, Zhao and Zou, 2020). Recent studies showed that control strategies based on occupancy information can save building energy by approximately 20–45%, and improve thermal comfort by 29.1% (Pang, Chen, Zhang, O'Neill, Cheng and Dong, 2020). Occupancy information ensures a closed-loop feedback strategy (Zou, Zhao, Yang and Wang, 2017) to control building heating, ventilation, and air-conditioning (HVAC) and lighting systems.

Vision-based occupancy detection to obtain accurate and robust occupancy information in buildings has recently become a hot research topic (Sun et al., 2020; Choi, Um, Kang, Kim and Kim, 2021b). Vision-based methods usually capture images/videos using cameras, and then apply image processing, video analysis, and deep learning technologies to sense people in buildings. These methods are mainly divided into three categories: body, face, and head detection. Head detection has been the perceived center point of people detection in complex indoor scenes. The limitations of body and face detection methods have gradually been exposed. Specifically, body detection methods extract the

body features for recognition, which suffers from inter-class and intra-class occlusions (Chi, Zhang, Xing, Lei, Li and Zou, 2020; Choi, Um, Kang, Kim and Kim, 2021a). Face detection methods rely on facial features; these methods fail when the person to be detected is not facing the camera. Compared with the former two methods, head detection has a wider range of applications because human heads are visible and reliable in complex indoor scenes. Indoor occupancy detection methods in buildings (Trivedi and Badarla, 2020; Zou et al., 2017; Sun, Zhao, Zhang and Hu, 2022) focus on the head part instead of the whole human body on account of the severe occlusion.

Although many head detectors have made great progress in general scenes (Vu, Osokin and Laptev, 2015; Granger, Kiran, Blais-Morin et al., 2017; Liu, Zhang, Xie, Wei, Wang and Niu, 2021a), the head detection task is still challenging in indoor scenes. As shown in Fig. 1, many background objects (e.g., black bags, balls, flowers) have head-like sizes, colors, and textures, resulting in a high false-positive rate (FPR). On the other hand, due to the relatively small scales, it is hard to detect heads with a high confidence score in crowded scenes. Moreover, moving heads cause significant variations in scale, pose, texture, and illumination, which increases the false-negative rate (FNR). Research on multi-scale features (Liu, Zhang, Bian, Zhang and Cheng, 2021b) and attention mechanisms (Woo, Park, Lee and Kweon, 2018; Shen, Qin and Zeng, 2019) aims to handle the multi-scale objects and similar background objects. However, existing studies mainly focus on head detection in static images (Meng, Li, Liu, Xu and Ji, 2020; Khan, Ullah, Uzair, Ullah, Ullah and Cheikh, 2019; Stewart, Andriluka and Ng, 2016), which is inadequate in indoor video scenarios.

*Corresponding author.

✉ sk118@mails.tsinghua.edu.cn (K. Sun);
ma-xt17@mails.tsinghua.edu.cn (X. Ma);
liup20@mails.tsinghua.edu.cn (P. Liu);
zhaogc@mail.tsinghua.edu.cn (Q. Zhao)
ORCID(s): 0000-0003-1648-3409 (K. Sun);
0000-0002-7250-6268 (X. Ma); 0000-0002-7952-5621 (Q. Zhao)

¹These authors contributed equally to this work.

Many video head detection approaches (Khan, Altamimi, Ullah, Ullah and Cheikh, 2020; Zou et al., 2017; Sundararaman, De Almeida Braga, Marchand and Pettre, 2021) aim to refine the final results by designing trackers and hand-crafted box-level rules between neighboring frames (Feichtenhofer, Pinz and Zisserman, 2017). But these box-level methods only rely on single detectors and are not optimized jointly (Wang, Zhou, Yan and Deng, 2018). Box-level methods would be inaccurate when the appearance of objects dramatically changes, especially as objects are occluded, or the interval between two nearby frames is large.

We notice that human heads are often in motion while the background objects are almost always static. To solve these issues, the following question needs to be answered: *can human head motion be utilized to enhance the features while suppressing background information?* This study gives us a confirmatory answer. The head motion information is captured by the pixel-wise difference between adjacent frames. The difference is sensitive to moving objects even though they are small in complex scenes. Besides, the motion information can be used to filter static objects. If static instances are suppressed while enhancing moving instances, the FPR and FNR can be effectively reduced.

We propose **Motion-aware Pseudo-Siamese Network (MPSN)** for indoor video head detection, an accurate and flexible framework for video head detection at the pixel level. It can robustly detect head regions in a sequence of frames, even when the time intervals of frames are large. First, we extract frame difference features between neighboring frames, which are sensitive to motion regions (see Fig. 1 for examples in the real dataset). Second, we propose a pseudo-siamese network to extract similar features between frame difference and the original image. Third, these features are aggregated with a constraint that can suppress false positives and recover false negatives. Finally, detection methods, such as region proposal network (RPN) (Ren, He, Girshick and Sun, 2015), are cascaded to generate proposal head boxes.

Besides, we utilize the pixel-level motion feature to guide the single-frame detector to propose robust head boxes. Unlike box-level methods (post-processing), our approach works at feature and pixel levels (pre-processing). Previous head detection approaches at feature or pixel levels are rare. To our best knowledge, MPSN is the first to jointly train the current frame and the pixel-level motion information into an end-to-end CNN network in head detection. This study aims to solve the indoor video head detection problems, such as similar static objects and diverse head samples. The contributions of this study are as follows: 1) We propose a pixel-level motion-aware pseudo-siamese network to learn the more robust head features. 2) With more effective motion features, we demonstrate MPSN on the crowd Brainwash dataset (Stewart et al., 2016) and the Restaurant dataset (El Ahmar, Erlik Nowruzi and Laganieri, 2020) with superior performance and low memory requirements. 3) As a general head detection framework, we demonstrate the flexibility of MPSN with different backbone networks (VGGNet16 (Simonyan and Zisserman, 2015), MobileNetv2 (Sandler,

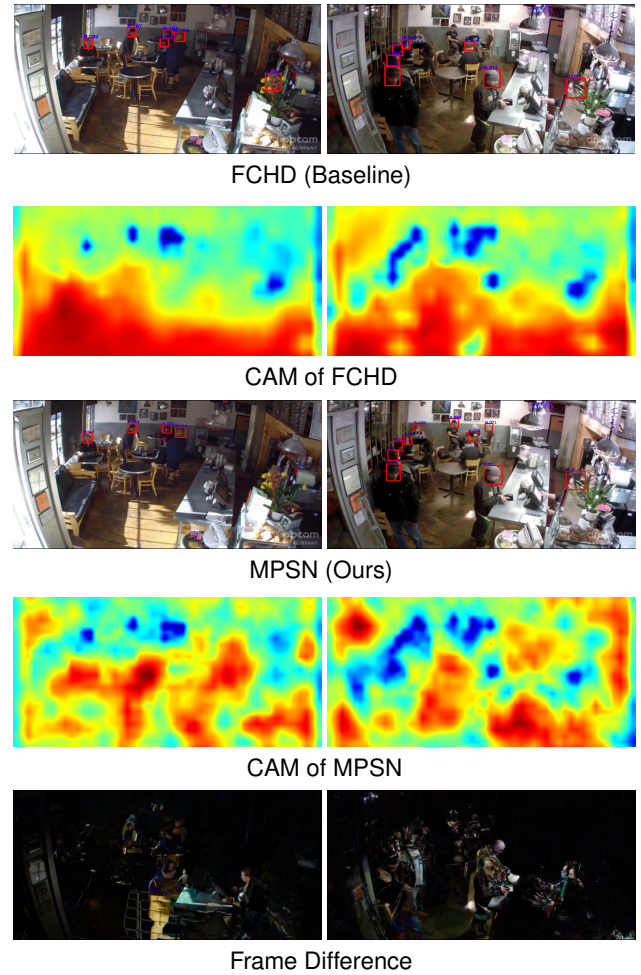


Figure 1: Comparison of MPSN with the baseline method FCHD (Meng et al., 2020). Two columns show two respective instances in the crowd Brainwash dataset (Stewart et al., 2016). In the first column, when similar objects (flowers) exist, MPSN can suppress the static regions and filter many false positives. In the second column, the single image detector fails to propose accurate boxes when heads are small. Our MPSN can enhance the motion regions and reduce many false negatives. For interpretation purposes, we visualize the features (heatmaps) of the last CNN layer, which are generated by the class activation map (CAM) method (Zhou et al., 2016). Deep blue regions of the heatmaps represent the locations of heads in the feature space.

Howard, Zhu, Zhmoginov and Chen, 2018), Resnet18 (He, Zhang, Ren and Sun, 2015)). 4) To evaluate the robustness of MPSN, we implement adversarial samples to MPSN, and provide the mathematical solution of small perturbations to select more robust models. 5) We apply MPSN to occupancy counting, which confirms its potential in practical building control systems.

2. RELATED WORK

2.1. Generic object detection

In recent years, deep learning technologies (e.g., CNN and transformer) have achieved state-of-the-art performances in object detection tasks. These CNN-based methods can be

divided into two categories: two-stage approach and one-stage approach. The two-stage methods, such as RCNN (Tien, Wei, Calautit, Darkwa and Wood, 2022) and R-FCN (Dai, Li, He and Sun, 2016), usually propose enough ROI (region of interest) boxes that contain potential objects, predict them as specific categories, and refine the offsets and scales of bounding boxes. The one-stage methods, such as YOLO (Choi et al., 2021a), SSD (Ke, Zhuang, Pu and Wang, 2020), and CenterNet (Duan, Bai, Xie, Qi, Huang and Tian, 2019), usually jointly predict the probability scores and regress bounding boxes together. The two-stage methods can achieve higher accuracy, while the one-stage methods have less computational complexity. Recently, DETR (Dai, Chen, Yang, Zhang, Yuan and Zhang, 2021) directly utilized transformer decoder and bipartite matching strategies to predict the joint class, position, and bounding boxes. However, transformer networks require a large number of training parameters and samples, which hinders their deployment in resource-constrained environments (Khan, Naseer, Hayat, Zamir, Khan and Shah, 2021).

2.2. Indoor occupancy detection

The applications of indoor occupancy detection methods include building energy saving, indoor environment comfort, and security management. Indoor occupancy detection is a challenging task involving people detection, video analysis, etc. Most Studies (Huang and Hao, 2020; Mutis, Ambekar and Joshi, 2020; Meng et al., 2020; Jacoby, Tan, Henze and Sarkar, 2021; Choi et al., 2021a) used general object detectors (YOLO, Faster RCNN, etc.) to detect indoor occupancy.

However, the indoor scenes are extremely complex owing to human bodies being occluded by desks, chairs, and other people (Sun et al., 2022; Choi et al., 2021a). Therefore, to avoid the severe occlusion problem, occupancy detection methods based on head detection have been developed (Meng et al., 2020; Zou et al., 2017; Guan and Huang, 2015; Acquah, Steele, Gokaraju, Tesiero and Monty, 2020). Object/head detection methods can be cascaded with video analysis technologies to obtain higher detection performance (Sun et al., 2022; Dino, Kalfaoglu, Sari, Akin, Iseri, Alatan, Kalkan and Erdogan, 2019).

2.3. Indoor head detection

Most related studies treat indoor head detection as a subtask of object detection. Early methods used hand-crafted features (Haar features (Viola and Jones, 2001), aggregate channel features (Chandran, Wong and Ieee, 2016), histogram of oriented gradients features (Zou et al., 2017), etc.) and classifiers to detect human heads. With the rapid development of deep learning, the mainstream of head detection method switched to CNN-based object detection methods (Stewart et al., 2016; Chouai, Dolezel, Stursa and Nemec, 2021; Khan, Ali, Zafar and Noorwali, 2020; Khan et al., 2020; Babu Sam, Surya and Venkatesh Babu, 2017).

In practice, different from generic objects, human heads have special properties. Thus, the specific anchor size selection strategy (Meng et al., 2020; Khan and Basalamah,

2021), multi-scale features aggregation strategy (Vu et al., 2015; Xiang and Zhu, 2017), attention selection strategy (Li, Wang, Wang, Tai, Qian, Yang, Wang, Li and Huang, 2019; Shen et al., 2019), and the relationship between heads and people matching strategy (Chi et al., 2020) can effectively improve detection performance.

3. METHODS

Given an image, we have a feature extraction network N_{feat} , and a detection network N_{det} . The output for input image I is $N_{det}(h)$, where $h = N_{feat}(I)$. The key concept of this study is to apply motion information to suppress static background objects and focus on the head instances at the pixel level.

The inference pipeline is depicted in Fig. 2, consisting of four modules: 1) The *motion estimation* module is developed to estimate the head motion information, which is fed to the pseudo-siamese network. 2) The *feature aggregation* module is proposed to extract robust head motion features. 3) The *gradient backpropagation* module which is presented in Appendix can explain the gradient principle of MPSN. 4) Finally, The *detection network* module decodes the aggregated features to head boxes.

3.1. Motion estimation

As mentioned in Section 1, the human head would not be static for a long time. We introduce prior motion knowledge to guide the network N_{feat} to extract effective head features. For further applications, we use simple background subtraction methods to roughly extract motion areas. We define the frame difference operator as

$$I_{df} = |I_f - I_{f-1}|, f = 1, \dots, N, \quad (1)$$

where I_f is the f th frame in an image sequence, and N is the sequence length. For color images, we conduct the same operation on three channels (RGB channels) by using Eq. (1), respectively. Although the time intervals between I_{f+1} and I_f have large variations in applications, this operator is sensitive to motion pixels and contains spatial location information.

Optical flow has been widely applied in video analysis. It helps to estimate video motion information. In this paper, we define the motion field by the optical flow estimation algorithm \mathcal{F} (Teed and Deng, 2020; Ilg, Mayer, Saikia, Keuper, Dosovitskiy and Brox, 2017; Lucas, Kanade et al., 1981) as

$$I_{df} = \mathcal{F}(I_f, I_{f-1}), f = 1, \dots, N, \quad (2)$$

The rough motion features will be further extracted by the following pseudo-siamese network.

3.2. Feature aggregation

The original frame I_f and frame difference image I_{df} are fed in parallel to the feature extraction network N_{feat} . In

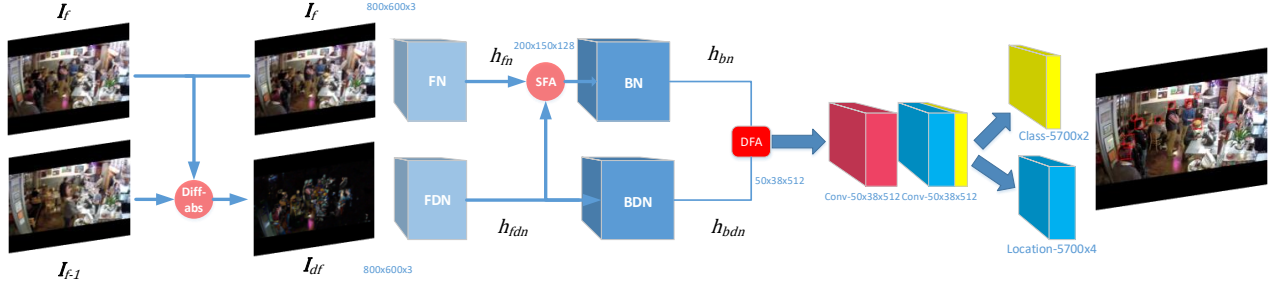


Figure 2: Framework of MPSN. Firstly, the original frame I_f and the frame difference I_{df} are fed in parallel to the pseudo-siamese network. The paired networks (FN and FDN, BN and BDN) have the same architectures but different weights. Secondly, the features are aggregated with our SFA and DFA at different pixel levels. Finally, the boxes and classes are predicted simultaneously with RPN.

other words, the inputs of the N_{feat} are two images, and the output is the aggregated features h_{agg} .

Many siamese CNN architectures can support the double inputs for similarity comparison (Wu, Zhang, Zhang, Zhang, Wang, Zhang and Sun, 2020) or regression (Held, Thrun and Savarese, 2016), whose weights are shared between the parallel streams. However, because the motion is specifically extracted defined in Eq. (1), I_{df} is different from the original frame I_f . Considering that they lie on different manifolds, the siamese CNN is not suitable for our task. We design a novel pseudo-siamese network (Hughes, Schmitt, Mou, Wang and Zhu, 2018) to handle this issue.

First, the pseudo-siamese network is used to extract similar features between I_f and I_{df} . The pseudo-siamese network can ensure the size and channel are completely equal at the same level layers. The architectures of the two sub-networks are totally the same, while the weights are learned separately. In Fig. 2, the front network (FN) corresponds to the front difference network (FDN) while the back network (BN) corresponds to the back difference network (BDN). Then, $N_{feat} = \{N_{FN}, N_{FDN}, N_{BN}, N_{BDN}\}$. The shape of features h_{fn} is equal to the features h_{fdn} 's:

$$\begin{aligned} h_{fn} &= N_{FN}(I_f) \\ h_{fdn} &= N_{FDN}(I_{df}). \end{aligned} \quad (3)$$

Second, to improve the accuracy and robustness of human head detection, the network should focus on moving areas that contain human heads. To enhance the motion regions and suppress the non-moving regions, we present shallow features aggregation (SFA) and deep features aggregation (DFA). The goal of the SFA is to aggregate the shallow features at the low-level layers. To reserve more temporal information, MPSN directly learns the sum of the two features after activation functions:

$$SFA : h_{fn} = h_{fdn} + h_{fn}. \quad (4)$$

Intuitively, the motion regions are added to the original features through this simple low-level aggregation. SFA can enhance the small and moving pixels but may be inaccurate when similar background objects exist. In fact, it is hard for SFA to ensure the activation scores of human heads are higher

than background objects'. To further enhance the moving instances and suppress the static background instances, we conduct the DFA on the position-sensitive score maps:

$$\begin{aligned} h_{bn} &= N_{BN}(h_{fn}) \\ h_{bdn} &= N_{BDN}(h_{fdn}) \\ DFA : h_{agg} &= \alpha \cdot h_{bn} \odot \sigma(h_{bdn}) + \beta \cdot h_{bdn}. \end{aligned} \quad (5)$$

In the deep layers, the instance-level features can represent head activation scores. The feature value of h_{bdn} represents the spatial intensity of moving heads. At every channel, we resize h_{bdn} with the sigmoid functions to (0, 1). The scores are multiplied with the features h_{bn} by element-wise (Hadamard) product in Eq. (5). In other words, the $\sigma(h_{bdn})$ can be seen as a special mask to activate the local regions of the original features maps h_{bn} . Unlike normal masks in image processing, this mask is dense and learnable: every value belongs to (0, 1) and is learned from the above pseudo-siamese network. This simple operator is powerful because the moving instances will be partly reserved while the static instances will be suppressed.

Note that $\beta \cdot h_{bdn}$ is added at the Eq. (5). Because the features h_{bdn} are resized to (0, 1) and the features h_{bn} are normalized (e.g., Batchnorm, Instancenorm, Layernorm) before activation functions, the activated head features will be decreased. To compensate for this loss and enhance the regions of moving heads, we add h_{bdn} after the element-wise product in Eq. (5).

3.3. Detection network

After obtaining the aggregated feature h_{agg} , we use a detector to get head proposals.

$$(c, t) = N_{det}(h_{agg}) \quad (6)$$

where output $t = (t_x, t_y, t_w, t_h)$ is a matrix that contains the parameterized coordinates of anchor boxes. t_x, t_y are the center coordinates of boxes, while t_w, t_h are the width and height of boxes. c is another matrix that contains class probabilities of anchor boxes. In the right of Fig. 2, our method will predict 5700 anchor boxes (50x38x3) in each image. c is marked as the yellow block, while t is marked as the blue block. Because the scales of heads are diverse,

we select three anchors of size 16x16, 32x32, and 64x64 to cover most heads. For each anchor, our method will predict 4 regression coordinates and 2 probability scores. Thus, the dimension of \mathbf{t} is 5700x4, while the dimension of \mathbf{c} is 5700x2.

On the other hand, to train the proposed network, the labels of head boxes need to be generated. We convert each ground-truth head box $G = (G_x, G_y, G_w, G_h)$ to parameterized coordinates $\hat{\mathbf{t}} = (\hat{t}_x, \hat{t}_y, \hat{t}_w, \hat{t}_h)$, through the following equation:

$$\begin{aligned}\hat{t}_x &= (G_x - B_x) / B_w \\ \hat{t}_y &= (G_y - B_y) / B_h \\ \hat{t}_w &= \log(G_w / B_w) \\ \hat{t}_h &= \log(G_h / B_h),\end{aligned}\quad (7)$$

where $B = (B_x, B_y, B_w, B_h)$ is one of the base anchors generated throughout the image (Girshick, Donahue, Darrell and Malik, 2014). By this equation, we can get the ground truth of coordinates $\hat{\mathbf{t}}$. On the other hand, the ground truth of classification $\hat{\mathbf{c}}$ can be generated directly by judging whether the anchor contains a head, i.e., 1 or 0.

Following the idea of RPN, we employ a multi-task loss function, as shown in Eq. (8).

$$y_f = L(\mathbf{c}, \mathbf{t}) = \frac{1}{N_s} \sum_i [L_{cla}(\mathbf{c}_i, \hat{\mathbf{c}}_i) + L_{box}(\mathbf{t}_i, \hat{\mathbf{t}}_i)]. \quad (8)$$

For each bounding box, $\hat{\mathbf{c}}$ is the ground truth of classification while $\hat{\mathbf{t}}$ is the ground truth of coordinates, as described above. i is the index of the bounding box. We expect to minimize the distance between each predicted anchor $(\mathbf{c}_i, \mathbf{t}_i)$ and the corresponding ground truth $(\hat{\mathbf{c}}_i, \hat{\mathbf{t}}_i)$. L_{cla} is the cross-entropy loss while L_{box} is the smooth L_1 loss. The loss terms are normalized by N_s , which is the number of positive samples. Moreover, the loss terms are computed only using positive samples. The positive samples are defined by three strategies: (1) An anchor which has Intersection over Union (IoU) overlap (Girshick et al., 2014) with ground truth ≥ 0.7 is a labeled positive sample. (2) Each ground truth has many IoUs with anchors, and we label the anchors corresponding to the maximum IoU as positive samples. (3) We restrict the number of positive samples ≤ 16 .

After defining the loss function, the backbone network and detector will be jointly trained end-to-end. The training hyperparameters are presented in Appendix.

4. EXPERIMENTS and DISCUSSION

First, we compare MPSN with various methods on two public indoor crowd datasets in Section 4.1. Considering that SFA, DFA can be embedded in most CNN-based models, we mainly focus on the flexibility and comparison study (in Section 4.2, 4.3, and 4.4). Based on different backbone networks and detectors, we show that MPSN can recover missed heads and filter the false background positives, giving a significant performance boosting. After comparison, we choose the best model to count indoor

Table 1

Comparison of MPSN against other methods on Brainwash dataset and Restaurant dataset.

Dataset	Method	Backbone	AP_{50}
Brainwash	ReInspect	GoogLeNet	0.78
	SSD	ResNet101	0.80
	DETR	ResNet18	0.53
	FCHD	VGGNet16	0.70
	CrowdDet	ResNet50	0.67
	Iter-E2EDET	ResNet50	0.52
	MPSN	MobileNetv2	0.90
	MPSN	VGGNet16	0.91
	YOLOX	CSPNet	0.83
Restaurant	HTC++	Swin-B	0.68
	SSD	ResNet18	0.51
	FCHD	VGGNet16	0.75
	CrowdDet	ResNet50	0.61
	Iter-E2EDET	ResNet50	0.61
	MPSN	MobileNetv2	0.84
	MPSN	VGGNet16	0.86

occupants, balancing the low computational complexity and high accuracy (in Section 4.5). In addition, adversarial samples are implemented to evaluate the robustness of MPSN (in Section 4.6). Finally, we also provide the mathematical solution of small perturbations to select more robust models.

4.1. Datasets

To evaluate MPSN, we test the publicly available Brainwash crowd dataset (Stewart et al., 2016) and Restaurant dataset (El Ahmar et al., 2020). For evaluation metrics, we use the standard average precision (AP_{50}). The Brainwash dataset includes 11917 images with 91146 labeled people, in which the test set contains 484 images. The Restaurant dataset was collected in four different indoor locations at a restaurant. It includes 1610 images, from which the test set contains 123 images. The images are extracted from the video with a large time interval, thus having significant diversity and difference. Fortunately, the camera was stable, and therefore the proposed motion estimation method is applicable.

4.2. Comparison with baselines

To compare to the state-of-the-art (SOTA) methods, we tested the AP of different methods on two datasets in Table 1. The detailed network architectures and hyperparameters are presented in Appendix.

The authors who published the Brainwash dataset (Stewart et al., 2016) provided a baseline detection method named ReInspect. SSD (Ke et al., 2020) algorithm uses multi-scale feature maps to achieve high detection accuracy. FCHD is a fast and accurate head detector with a specific anchor size selection strategy. HTC++ framework (Chen, Pang, Wang, Xiong, Li, Sun, Feng, Liu, Shi, Ouyang et al., 2019) combines detection and segmentation tasks into a joint multi-stage processing and utilizes spatial context to further boost the performance. YOLOX (Ge, Liu, Wang, Li and Sun,

Table 2

Comparison of MPSN against the single frame and two frames method among different backbones on two datasets.

Dataset	Method	VGGNet16	MobileNetv2	ResNet18
Brainwash	Single frame	0.876	0.828	0.855
	Two frames	0.868	0.821	0.857
	MPSN	0.878	0.890	0.885
Restaurant	Single frame	0.750	0.785	0.769
	Two frames	0.782	0.808	0.768
	MPSN	0.857	0.838	0.802
Parameters		123.8M	6.7M	24.9M
Inference time		149ms	125ms	109ms

2021) is a high-performance anchor-free detector through integrating YOLO series. CrowdDet (Chu, Zheng, Zhang and Sun, 2020) is a SOTA detector that achieves 0.907 AP performance in the challenging CrowdHuman dataset. To simplify detection pipelines and bypass surrogate tasks, DETR directly utilizes the transformer for object sequence prediction. Iter-E2EDET (Zheng, Zhang, Zhang, Qi and Sun, 2022) is a SOTA people detector and achieves the highest accuracy in the CrowdHuman detection task¹ so far.

Compared with the prior methods, our proposed method, MPSN, achieved the best performance accuracy in both datasets. Considering that the MobileNetv2 backbone (Sandler et al., 2018) has fewer parameters and lower computational complexity, we used it as the default backbone in further discussion.

4.3. Flexibility of MPSN

To sufficiently evaluate the flexibility, we conducted three experiments based on FCHD. Table 2 summarizes the performance on two datasets. We selected the best model on the evaluation dataset ($valAP_{50}$) and tested this model on the test dataset ($testAP_{50}$).

- Single frame: training the general model with single frame as the input.
- Two frames: training the pseudo-siamese model with two adjacent frames (I_f, I_{f-1}). In this situation, the DFA degenerates to $h_{agg} = h_{bn} + h_{bdn}$.
- Diffabs: using pre-computed sequence pairs (I_f, I_{df}) to train the pseudo-siamese model with the f -th frame ground truth.
- DFA: two variants of DFA are considered, where \odot represents using our Eq. (5) to aggregate the deep features, and \oplus represents using the simple addition.

We tested MPSN with different backbone networks (VGGNet16, MobileNetv2, Resnet18). In each backbone network and dataset, we fixed hyperparameters to fairly compare single frame, two frames, and MPSN methods. The results in Table 2 show MPSN achieved superior performance

¹<https://paperswithcode.com/sota/object-detection-on-crowdhuman-full-body>

Table 3

Ablation with DETR on the Brainwash dataset.

Input	SFA	DFA	$valAP_{50}$	$testAP_{50}$	Params
Single frame			0.509	0.525	344.9M
Two frames		\oplus	0.783	0.713	477.8M
Diffabs		\oplus	0.723	0.713	389.7M
Diffabs		\odot	0.774	0.762	477.8M

Table 4

Comparison of Diffabs against Flow on the two datasets.

Dataset	Network	Flow		Diffabs	
		$valAP_{50}$	$testAP_{50}$	$valAP_{50}$	$testAP_{50}$
Restaurant	VGGNet16	0.789	0.812	0.816	0.857
	MobileNetv2	0.759	0.790	0.752	0.838
	Resnet18	0.743	0.793	0.747	0.802
Brainwash	VGGNet16	0.866	0.903	0.884	0.909
	MobileNetv2	0.865	0.880	0.867	0.899
	Resnet18	0.850	0.880	0.852	0.885

on two datasets. It means that MPSN does not rely on fixed network architectures, thus it can be flexibly applied in each CNN-based detection framework with high accuracy. We also compare computational complexity of MPSN with different backbone networks in Table 2. It can be seen that, MPSN with MobileNetv2 has smaller parameters while MPSN with ResNet18 has faster inference speed.

As for "MobileNetv2" on the Restaurant dataset, the single frame method achieved a reasonable performance of 0.785 AP. Simultaneously, the two frames method achieved similar accuracy of 0.808 AP. After applying MPSN, we achieve an AP of 0.838 with the same hyperparameters. This significant improvement means that MPSN can guide CNN to extract motion features effectively, resulting in higher accuracy.

To verify the flexibility, we also applied our MPSN to DETR framework, which detects objects using a transformer. The DETR with ResNet18 is compared in Table 3. In our experiments, we only added DFA in the ResNet18 backbone network before the transformer decoder. The Diffabs and two frames methods (0.713 AP) were significantly improved. It means that the additional information can help the performance. Importantly, compared with the two frames situation at the same scale of model parameters, our Diffabs and DFA method achieved 0.762 AP, about 6.87% improvement. It benefits from the crafty design of DFA and the effective use of motion information. However, the transformer decoder has more parameters, which makes it not applicable in practice. In contrast, since the MobileNetv2 backbone network has fewer parameters and computational complexity (Sandler et al., 2018), it is suitable for edge deployments.

4.4. Diffabs versus Flow

Optical flow is widely used in video analysis and processing. We compare optical flow and frame difference in this part. We used SOTA optical flow estimation method named RAFT (Teed and Deng, 2020) to extract flow images, which

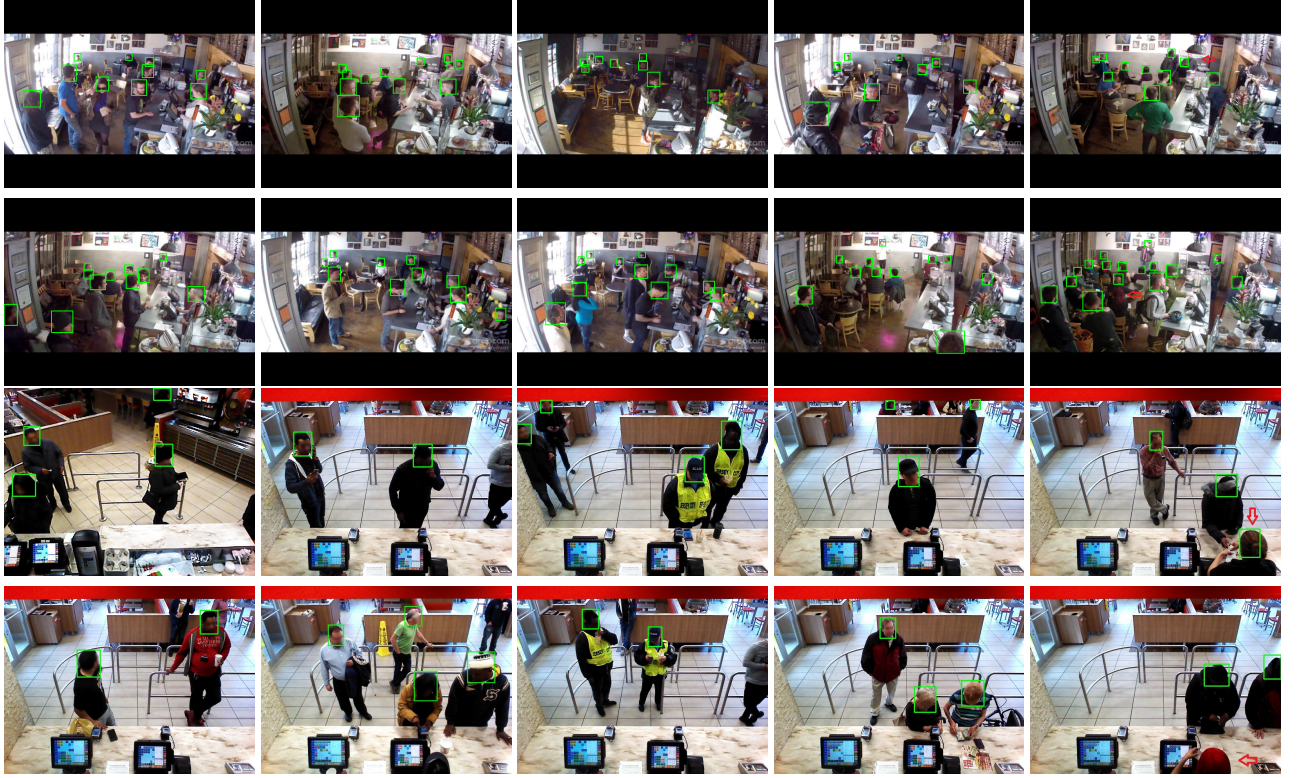


Figure 3: Qualitative results of MPSN on test set of Brainwash dataset and Restaurant dataset. In the first four columns, we present successful results where all human heads are detected accurately even though several heads are tiny. In the last column, we provide some failure instances. As marked by red arrows in the pictures, four heads are missed. In the top-right figure, the man is occluded by a bright lamp and another person. In the second right figure, the back-view woman with red hair is missed because her hair color is close to near pixels. They are hard to be discovered even with human eyes. In the third right figure, the head is not located accurately. In the bottom right figure, the person is missed. Two potential reasons: only part head can be seen; heads with red cap in datasets are rare.

are the inputs to our MPSN. The frame difference was simply implemented by subtraction and absolute value operators. In this experiment, we fixed DFA, and hyperparameters to compare Diffabs and Flow fairly. The results are shown in Table 4. Diffabs achieved better performance than Flow in most situations, regardless of datasets and backbone networks. Note that the SOTA optical flow estimation method has more complex computation and more parameters than the simple frame difference method. In conclusion, as compared to Flow-based methods, the Diffabs-based methods have lower computational requirements while enjoying higher accuracy.

4.5. An application: occupancy counting

An application of MPSN is occupancy counting, which is the core component of occupancy-based control in buildings. As a critical perception algorithm, MPSN provides the number of occupants, which can be applied to control the HVAC and lighting systems. For example, energy can be effectively saved and indoor air environment quality can be improved, through adjusting the opening rate of air dampers dynamically according to the number of people in the building. In this experiment, we applied MPSN to evaluate the performance of indoor occupancy counting. (In

practice, balancing the low computational complexity and high accuracy, we chose the MobileNetv2 backbone as the test model.)

We define two evaluation indicators for occupancy counting as follows:

$$NMAE = \frac{1}{N} \sum_{f=1}^N \frac{|n_f - \bar{n}_f|}{n_f + \bar{n}_f}, \quad (9)$$

$$SCORE = \frac{1}{N} \sum_{f=1}^N (1 - \text{sign}|n_f - \bar{n}_f|),$$

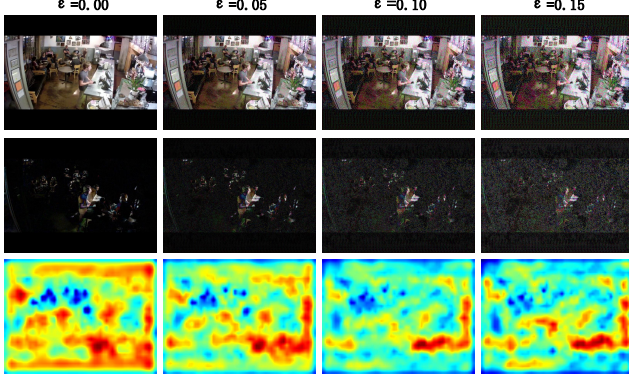
where n_f represents the true number of people (ground truth) in the f_{th} frame. And \bar{n}_f represents the predicted number of people (predicted value) in the f_{th} frame. The ground truth of the video is obtained manually, while the predicted value is output by MPSN. *sign* represents the sign function.

The normalized mean absolute error ($NMAE \in [0, 1]$) is calculated through the absolute difference between n_f and \bar{n}_f . We normalized it because the occupancy counting error increases with the number of people (Sun et al., 2020). SCORE (hit rate) is the ratio of ground truth equal to the predicted value. We expect NMAE to be smaller and SCORE

Table 5

Performance of occupancy counting.

Dataset	NMAE	SCORE	Avg head counting
Restaurant	0.125	0.525	2.549
Brainwash	0.125	0.186	10.345

**Figure 4:** Visualization of effects of increasing adversarial perturbation. First row represents adversarial images; second row represents motion in adversarial images; last row represents CAM heatmaps from the last CNN layer.

to be bigger. Note that the occupancy counting application mainly focuses on the number of occupants in buildings. Thus, we assume the detected occupancy boxes match the ground truth position in Eq. (9).

In Table 5, the Avg head counting is the average occupancy counting in the test dataset. NMAE does not change even though the average numbers of people are significantly different in the two datasets. It partially shows that our NMAE is insensitive to the scale of occupants. On the other hand, the small NMAE indicates that MPSN has a good performance in occupancy counting, as shown in Fig. 3. Intuitively, if the true number of people (n_f) is 5, with the 0.125 NMAE, the predicted number (\bar{n}_f) will be 4 or 6 statistically. This small error can be tolerated for coarse-grained building control. Note that MPSN is only a head detector, thus post-processing and pre-processing methods are able to cascaded to improve the counting performance. These processing methods (such as max counting algorithm (Choi et al., 2021a), clustering analyzer (Zou et al., 2017) and occupancy frequency histogram (Sun et al., 2022)) are beyond the scope of this paper.

4.6. Robustness to adversarial samples

Recent studies on adversarial samples (Akhtar and Mian, 2018) found that imperceptible perturbations in input images can completely fool the deep learning models. We conducted an experiment on robustness with adversarial samples. Instead of defending the adversarial attacks, the purpose of this experiment was to evaluate the robustness of MPSN. We added adversarial perturbations to our dataset,

which are computed by the fast gradient sign method (FGSM) (Goodfellow, Shlens and Szegedy, 2015):

$$\begin{aligned} I_f^a &= I_f + \epsilon \text{sign}(\nabla_{I_f} L(\theta, I_f, y_f)), \\ I_{f-1}^a &= I_{f-1} + \epsilon \text{sign}(\nabla_{I_{f-1}} L(\theta, I_{f-1}, y_{f-1})), \end{aligned} \quad (10)$$

where $\epsilon \in [0, 1]$. In Fig. 5, with the ϵ increasing, the attack effect also increases; thus the AP_{50} decreases. It is worth noting that the AP_{50} of MPSN is always higher than FCHD for different ϵ . It means that no matter how great this attack is, MPSN can achieve a better performance compared with FCHD. At $\epsilon = 0$ level, the attack effects disappear. At $\epsilon = 0.4$ level, MPSN converges to higher accuracy. Detailed effects against adversarial perturbations are visualized in Fig. 4. To some extent, the blue areas in heatmaps can represent the head positions. With the increasing perturbations, the heatmaps become inaccurate, which confirms the decrease of AP in Fig. 5. However, it looks like that the second row (frame difference) is less affected by the perturbations because the motion area is significant. Perhaps it reduces the perturbations and results in higher accuracy in Fig. 5.

We used the Non-I.I.D. Index (NI) (He, Shen and Cui, 2021) to evaluate the robustness in Fig. 5:

$$\begin{aligned} NI_{MPSN} &= \left\| \frac{\overline{g_\theta(I^a, I_d^a)} - \overline{g_\theta(I, I_d)}}{\text{std}(g_\theta(I^a, I_d^a) \cup g_\theta(I, I_d))} \right\|_2, \\ NI_{FCHD} &= \left\| \frac{\overline{g_\varphi(I^a)} - \overline{g_\varphi(I)}}{\text{std}(g_\varphi(I^a) \cup g_\varphi(I))} \right\|_2, \end{aligned} \quad (11)$$

and

$$\begin{aligned} \overline{g_\theta(I^a, I_d^a)} &= \frac{1}{N} \sum_{f=1}^N g_\theta(I_f^a, I_{df}^a), \\ \overline{g_\varphi(I^a)} &= \frac{1}{N+1} \sum_{f=0}^N g_\varphi(I_f^a), \end{aligned} \quad (12)$$

where g_θ represents the feature extractor of MPSN and g_φ represents the feature extractor of FCHD. The superscript a represents the input image after attack, $\overline{(\cdot)}$ represents the first order moment, std is the standard deviation function and $\|\cdot\|_2$ represents the 2-norm. Eq. (11) measures the feature difference between original images and adversarial samples.

Since MPSN and FCHD have different network architectures, we slightly modified the NI as follows:

$$\begin{aligned} NI_{MPSN} &= \left\| \frac{\overline{CAM(h_{det}^a)} - \overline{CAM(h_{det})}}{\text{std}(CAM(h_{det}^a) \cup CAM(h_{det}))} \right\|_2, \\ NI_{FCHD} &= \left\| \frac{\overline{CAM(d_{det}^a)} - \overline{CAM(d_{det})}}{\text{std}(CAM(d_{det}^a) \cup CAM(d_{det}))} \right\|_2, \end{aligned} \quad (13)$$

where h_{det} and d_{det} represent the features from the last CNN layer of MPSN and FCHD, respectively. The main

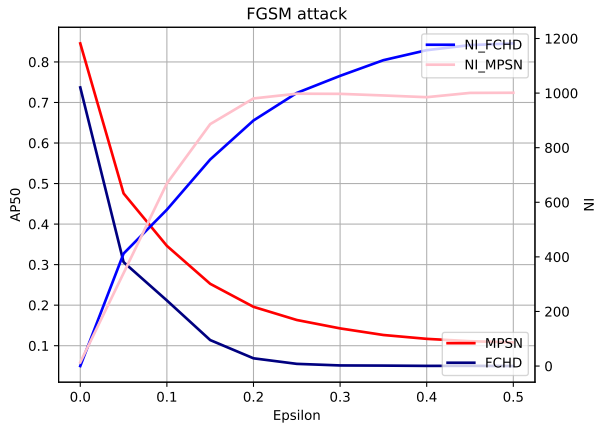


Figure 5: Comparison of robustness between MPSN and FCHD under adversarial noise.

advantage of *CAM* is interpretability. Thus we specify the *CAM* heatmap from the last CNN layer as $g(\cdot)$ function.

The comparison results are shown in Fig. 5. The strong correlation between NI and testing error was proved in (He et al., 2021). It seems that FCHD is more robust than MPSN if $\epsilon \in [0.07, 0.25]$. It can be explained that the AP decrease of MPSN is serious. However, in applications, we focus on the small ϵ because the great perturbations violate small input changes and even destroy the original image (Feinman, Curtin, Shintre and Gardner, 2017). According to Fig. 5, if $\epsilon \leq 0.07$, MPSN is more robust and accurate than FCHD. In this situation, we are more likely to apply MPSN in real systems. On the other hand, if $\epsilon \geq 0.07$, we may choose FCHD. Therefore, the threshold is very important in selecting the more robust model and further guide the applications. While the threshold is experimental, we further discuss the mathematical solution of the small ϵ in the Appendix.

5. CONCLUSIONS

In this study, we present MPSN to suppress false positives and recover missed detection in video head detection. We design SFA and DFA by introducing motion information, guiding the pseudo-siamese model to extract robust head motion features. Experimental results show that MPSN achieves higher performance on two challenging datasets. Experiments based on different backbone networks (VGGNet16, MobileNetv2, Resnet18) verify the flexibility of MPSN. Compared with optical flow-based methods, our Diffabs-based methods have lower computational requirements and higher accuracy in experiments. Adversarial samples are implemented to evaluate the robustness of MPSN. We also provide the mathematical solution of small perturbations to select more robust models.

Many studies have applied vision-based occupancy detection methods for occupancy-centric controls (OCC). Differently, this study provides new thinking to stabilize the detection and improve performance, filling the gap in video head detection at the pixel level. Through suppressing static background objects and enhancing moving occupants, MPSN is more robust and accurate, solving two essential problems

(the false positive rate and false-negative rate) in building occupancy measurement to some extent. Besides, we try to open the black boxes of deep CNN and provide a detailed perturbation analysis in Appendix. Our experiments show a large potential in energy-saving and indoor environment comfort. A limitation of MPSN is that the time interval of adjacent frames is a constant. In the future, we would distill and deploy MPSN in edge devices (e.g., Raspberry Pi and Jetson Nano) in buildings. We hope our study can promote the application of the deep learning model in real-world building occupancy measurement.

6. ACKNOWLEDGMENTS

This work was supported by the National Natural Science Foundation of China under Grant 62192751 and 61425027, in part by the National Key Research and Development Project of China under Grant 2017YFC0704100, and 2016YFB0901900, in part by the 111 International Collaboration Program of China under Grant BP2018006, in part by the BNRist Program under Grant No. BNR2019TD01009, and in part by China National Innovation Center of High Speed Train Project Under Grant CX/KJ-2020-0006.

We sincerely appreciate reviewers, whose valuable comments have benefited our paper significantly!

References

- Acquaah, Y., Steele, J.B., Gokaraju, B., Tesiero, R., Monty, G.H., 2020. Occupancy detection for smart hvac efficiency in building energy: A deep learning neural network framework using thermal imagery, in: 2020 IEEE Applied Imagery Pattern Recognition Workshop (AIPR), IEEE. pp. 1–6.
- Akhtar, N., Mian, A., 2018. Threat of adversarial attacks on deep learning in computer vision: A survey. *Ieee Access* 6, 14410–14430.
- Babu Sam, D., Surya, S., Venkatesh Babu, R., 2017. Switching convolutional neural network for crowd counting, in: Proceedings of the IEEE conference on computer vision and pattern recognition, pp. 5744–5752.
- Chandran, A.K., Wong, W.C., Ieee, 2016. Pedestrian Crowd Level Estimation by Head Detection using Bio-inspired Retina Model. *Proceedings of the 2016 Ieee Region 10 Conference*.
- Chen, K., Pang, J., Wang, J., Xiong, Y., Li, X., Sun, S., Feng, W., Liu, Z., Shi, J., Ouyang, W., et al., 2019. Hybrid task cascade for instance segmentation, in: Proceedings of the IEEE/CVF Conference on Computer Vision and Pattern Recognition, pp. 4974–4983.
- Chi, C., Zhang, S., Xing, J., Lei, Z., Li, S.Z., Zou, X., 2020. Relational learning for joint head and human detection, in: Proceedings of the AAAI Conference on Artificial Intelligence, pp. 10647–10654.
- Choi, H., Um, C.Y., Kang, K., Kim, H., Kim, T., 2021a. Application of vision-based occupancy counting method using deep learning and performance analysis. *Energy and Buildings* 252, 111389.
- Choi, H., Um, C.Y., Kang, K., Kim, H., Kim, T., 2021b. Review of vision-based occupant information sensing systems for occupant-centric control. *Building and Environment* 203, 108064.
- Chouai, M., Dolezel, P., Stursa, D., Nemecek, Z., 2021. New end-to-end strategy based on deeplabv3+ semantic segmentation for human head detection. *Sensors* 21, 5848.
- Chu, X., Zheng, A., Zhang, X., Sun, J., 2020. Detection in crowded scenes: One proposal, multiple predictions, in: Proceedings of the IEEE/CVF Conference on Computer Vision and Pattern Recognition (CVPR).
- Dai, J., Li, Y., He, K., Sun, J., 2016. R-fcn: Object detection via region-based fully convolutional networks. *Advances in neural information processing systems* 29.

- Dai, X., Chen, Y., Yang, J., Zhang, P., Yuan, L., Zhang, L., 2021. Dynamic detr: End-to-end object detection with dynamic attention, in: Proceedings of the IEEE/CVF International Conference on Computer Vision, pp. 2988–2997.
- Dino, I., Kalfaoglu, E., Sari, A., Akin, S., Iseri, O., Alatan, A., Kalkan, S., Erdogan, B., 2019. Video content analysis-based detection of occupant presence for building energy modelling. *Advances in ICT in Design, Construction and Management in Architecture, Engineering, Construction and Operations (AECO)*, Northumbria University (9 2019), 974–985.
- Duan, K., Bai, S., Xie, L., Qi, H., Huang, Q., Tian, Q., 2019. Centernet: Keypoint triplets for object detection, in: Proceedings of the IEEE/CVF international conference on computer vision, pp. 6569–6578.
- El Ahmar, W.A., Erlik Nowruz, F., Laganier, R., 2020. Fast human head and shoulder detection using convolutional networks and rgb data, in: 2020 IEEE/CVF Conference on Computer Vision and Pattern Recognition Workshops (CVPRW), pp. 479–487. doi:10.1109/CVPRW50498.2020.00061.
- Feichtenhofer, C., Pinz, A., Zisserman, A., 2017. Detect to track and track to detect, in: 2017 IEEE International Conference on Computer Vision (ICCV), pp. 3057–3065. doi:10.1109/ICCV.2017.330.
- Feinman, R., Curtin, R.R., Shintre, S., Gardner, A.B., 2017. Detecting adversarial samples from artifacts. *arXiv:1703.00410*.
- Ge, Z., Liu, S., Wang, F., Li, Z., Sun, J., 2021. YOLOX: exceeding YOLO series in 2021. *CoRR abs/2107.08430*. URL: <https://arxiv.org/abs/2107.08430>, *arXiv:2107.08430*.
- Girshick, R., Donahue, J., Darrell, T., Malik, J., 2014. Rich feature hierarchies for accurate object detection and semantic segmentation, in: 2014 IEEE Conference on Computer Vision and Pattern Recognition, pp. 580–587. doi:10.1109/CVPR.2014.81.
- Goodfellow, I.J., Shlens, J., Szegedy, C., 2015. Explaining and harnessing adversarial examples. *arXiv:1412.6572*.
- Granger, E., Kiran, M., Blais-Morin, L.A., et al., 2017. A comparison of cnn-based face and head detectors for real-time video surveillance applications, in: 2017 Seventh International Conference on Image Processing Theory, Tools and Applications (IPTA), IEEE, pp. 1–7.
- Guan, Y., Huang, Y., 2015. Multi-pose human head detection and tracking boosted by efficient human head validation using ellipse detection. *Engineering Applications of Artificial Intelligence* 37, 181–193. URL: <https://www.sciencedirect.com/science/article/pii/S0952197614002036>, doi:https://doi.org/10.1016/j.engappai.2014.08.004.
- He, K., Zhang, X., Ren, S., Sun, J., 2015. Deep residual learning for image recognition. *CoRR abs/1512.03385*. URL: <http://arxiv.org/abs/1512.03385>, *arXiv:1512.03385*.
- He, Y., Shen, Z., Cui, P., 2021. Towards non-i.i.d. image classification: A dataset and baselines. *Pattern Recognition* 110, 107383. URL: <https://www.sciencedirect.com/science/article/pii/S0031320320301862>, doi:https://doi.org/10.1016/j.patcog.2020.107383.
- Held, D., Thrun, S., Savarese, S., 2016. Learning to track at 100 fps with deep regression networks, in: European conference on computer vision, Springer, pp. 749–765.
- Huang, Q., Hao, K., 2020. Development of cnn-based visual recognition air conditioner for smart buildings. *J. Inf. Technol. Constr.* 25, 361–373.
- Hughes, L.H., Schmitt, M., Mou, L., Wang, Y., Zhu, X.X., 2018. Identifying corresponding patches in sar and optical images with a pseudo-siamese cnn. *IEEE Geoscience and Remote Sensing Letters* 15, 784–788.
- Ilg, E., Mayer, N., Saikia, T., Keuper, M., Dosovitskiy, A., Brox, T., 2017. FlowNet 2.0: Evolution of optical flow estimation with deep networks, in: Proceedings of the IEEE conference on computer vision and pattern recognition, pp. 2462–2470.
- Jacoby, M., Tan, S.Y., Henze, G., Sarkar, S., 2021. A high-fidelity residential building occupancy detection dataset. *Scientific Data* 8, 280. URL: <https://doi.org/10.1038/s41597-021-01055-x>, doi:10.1038/s41597-021-01055-x.
- Ke, R., Zhuang, Y., Pu, Z., Wang, Y., 2020. A smart, efficient, and reliable parking surveillance system with edge artificial intelligence on iot devices. *IEEE Transactions on Intelligent Transportation Systems* 22, 4962–4974.
- Khan, S., Naseer, M., Hayat, M., Zamir, S.W., Khan, F.S., Shah, M., 2021. Transformers in vision: A survey. *ACM Computing Surveys (CSUR)*.
- Khan, S.D., Ali, Y., Zafar, B., Noorwali, A., 2020. Robust head detection in complex videos using two-stage deep convolution framework. *IEEE Access* 8, 98679–98692.
- Khan, S.D., Altamimi, A.B., Ullah, M., Ullah, H., Cheikh, F.A., 2020. TCM: Temporal Consistency Model for Head Detection in Complex Videos. *JOURNAL OF SENSORS* 2020. doi:10.1155/2020/8861296.
- Khan, S.D., Basalamah, S., 2021. Multi-scale person localization with multi-stage deep sequential framework. *International Journal of Computational Intelligence Systems* 14, 1217–1228. URL: <https://doi.org/10.2991/ijcis.d.210326.001>, doi:https://doi.org/10.2991/ijcis.d.210326.001.
- Khan, S.D., Ullah, H., Uzair, M., Ullah, M., Ullah, R., Cheikh, F.A., 2019. Density independent and scale aware model for crowd counting and localization, pp. 4474–4478.
- Li, J., Wang, Y., Wang, C., Tai, Y., Qian, J., Yang, J., Wang, C., Li, J., Huang, F., 2019. Dsfd: dual shot face detector, in: Proceedings of the IEEE/CVF Conference on Computer Vision and Pattern Recognition, pp. 5060–5069.
- Liu, J., Zhang, Y., Xie, J., Wei, Y., Wang, Z., Niu, M., 2021a. Head detection based on dr feature extraction network and mixed dilated convolution module. *Electronics* 10, 1565.
- Liu, Y., Zhang, X.Y., Bian, J.W., Zhang, L., Cheng, M.M., 2021b. Samnet: Stereoscopically attentive multi-scale network for lightweight salient object detection. *IEEE Transactions on Image Processing* 30, 3804–3814.
- Lucas, B.D., Kanade, T., et al., 1981. An iterative image registration technique with an application to stereo vision, Vancouver, British Columbia.
- Meng, Y.b., Li, T.y., Liu, G.h., Xu, S.j., Ji, T., 2020. Real-time dynamic estimation of occupancy load and an air-conditioning predictive control method based on image information fusion. *Building and Environment* 173, 106741.
- Mutis, I., Ambekar, A., Joshi, V., 2020. Real-time space occupancy sensing and human motion analysis using deep learning for indoor air quality control. *Automation in Construction* 116, 103237. URL: <https://www.sciencedirect.com/science/article/pii/S0926580519307630>, doi:https://doi.org/10.1016/j.autcon.2020.103237.
- Pang, Z., Chen, Y., Zhang, J., O'Neill, Z., Cheng, H., Dong, B., 2020. Nationwide hvac energy-saving potential quantification for office buildings with occupant-centric controls in various climates. *Applied Energy* 279, 115727. URL: <https://www.sciencedirect.com/science/article/pii/S0306261920312186>, doi:https://doi.org/10.1016/j.apenergy.2020.115727.
- Ren, S., He, K., Girshick, R., Sun, J., 2015. Faster r-cnn: Towards real-time object detection with region proposal networks. *Advances in neural information processing systems* 28.
- Rueda, L., Agbossou, K., Cardenas, A., Henao, N., Kelouwani, S., 2020. A comprehensive review of approaches to building occupancy detection. *Building and Environment* 180, 106966. URL: <https://www.sciencedirect.com/science/article/pii/S0360132320303255>, doi:https://doi.org/10.1016/j.buildenv.2020.106966.
- Russakovsky, O., Deng, J., Su, H., Krause, J., Satheesh, S., Ma, S., Huang, Z., Karpathy, A., Khosla, A., Bernstein, M., Berg, A.C., Fei-Fei, L., 2015. ImageNet Large Scale Visual Recognition Challenge. *International Journal of Computer Vision (IJCV)* 115, 211–252. doi:10.1007/s11263-015-0816-y.
- Sandler, M., Howard, A.G., Zhu, M., Zhmoginov, A., Chen, L., 2018. Inverted residuals and linear bottlenecks: Mobile networks for classification, detection and segmentation. *CoRR abs/1801.04381*.
- Shen, W., Qin, P., Zeng, J., 2019. An indoor crowd detection network framework based on feature aggregation module and hybrid attention selection module, in: Proceedings of the IEEE/CVF International

- Conference on Computer Vision Workshops, pp. 0–0.
- Simonyan, K., Zisserman, A., 2015. Very deep convolutional networks for large-scale image recognition, in: International Conference on Learning Representations.
- Stewart, R., Andriluka, M., Ng, A.Y., 2016. End-to-end people detection in crowded scenes, in: Proceedings of the IEEE conference on computer vision and pattern recognition, pp. 2325–2333.
- Sun, K., Zhao, Q., Zhang, Z., Hu, X., 2022. Indoor occupancy measurement by the fusion of motion detection and static estimation. *Energy and Buildings* 254, 111593. URL: <https://www.sciencedirect.com/science/article/pii/S037877882100877X>, doi:<https://doi.org/10.1016/j.enbuild.2021.111593>.
- Sun, K., Zhao, Q., Zou, J., 2020. A review of building occupancy measurement systems. *Energy and Buildings* 216, 109965. URL: <https://www.sciencedirect.com/science/article/pii/S0378778819332918>, doi:<https://doi.org/10.1016/j.enbuild.2020.109965>.
- Sundaraman, R., De Almeida Braga, C., Marchand, E., Pettre, J., 2021. Tracking pedestrian heads in dense crowd, in: Proceedings of the IEEE/CVF Conference on Computer Vision and Pattern Recognition (CVPR), pp. 3865–3875.
- Teed, Z., Deng, J., 2020. Raft: Recurrent all-pairs field transforms for optical flow, in: European conference on computer vision, Springer. pp. 402–419.
- Tien, P.W., Wei, S., Calautit, J.K., Darkwa, J., Wood, C., 2022. Real-time monitoring of occupancy activities and window opening within buildings using an integrated deep learning-based approach for reducing energy demand. *Applied Energy* 308, 118336. URL: <https://www.sciencedirect.com/science/article/pii/S0306261921015865>, doi:<https://doi.org/10.1016/j.apenergy.2021.118336>.
- Trivedi, D., Badarla, V., 2020. Occupancy detection systems for indoor environments: A survey of approaches and methods. *Indoor and Built Environment* 29, 1053–1069.
- Viola, P., Jones, M., 2001. Rapid object detection using a boosted cascade of simple features, in: Proceedings of the 2001 IEEE Computer Society Conference on Computer Vision and Pattern Recognition. CVPR 2001, pp. I–511–18 vol.1.
- Vu, T.H., Osokin, A., Laptev, I., 2015. Context-aware CNNs for person head detection, in: 2015 IEEE INTERNATIONAL CONFERENCE ON COMPUTER VISION (ICCV), pp. 2893–2901. IEEE International Conference on Computer Vision, Santiago, CHILE, DEC 11-18, 2015.
- Wang, S., Zhou, Y., Yan, J., Deng, Z., 2018. Fully motion-aware network for video object detection, in: Ferrari, V., Hebert, M., Sminchisescu, C., Weiss, Y. (Eds.), *Computer Vision – ECCV 2018*, Springer International Publishing, Cham. pp. 557–573.
- Woo, S., Park, J., Lee, J.Y., Kweon, I.S., 2018. Cbam: Convolutional block attention module, in: Proceedings of the European conference on computer vision (ECCV), pp. 3–19.
- Wu, C., Zhang, Y., Zhang, Y., Zhang, W., Wang, H., Zhang, Y., Sun, X., 2020. Motion guided siamese trackers for visual tracking. *IEEE Access* 8, 7473–7489. doi:10.1109/ACCESS.2020.2964269.
- Xiang, J., Zhu, G., 2017. Joint face detection and facial expression recognition with mtcnn, in: 2017 4th international conference on information science and control engineering (ICISCE), IEEE. pp. 424–427.
- Zheng, A., Zhang, Y., Zhang, X., Qi, X., Sun, J., 2022. Progressive End-to-End Object Detection in Crowded Scenes. *arXiv e-prints*, arXiv:2203.07669arXiv:2203.07669.
- Zhou, B., Khosla, A., Lapedriza, A., Oliva, A., Torralba, A., 2016. Learning deep features for discriminative localization, in: Proceedings of the IEEE conference on computer vision and pattern recognition, pp. 2921–2929.
- Zou, J., Zhao, Q., Yang, W., Wang, F., 2017. Occupancy detection in the office by analyzing surveillance videos and its application to building energy conservation. *Energy and Buildings* 152, 385–398. doi:10.1016/j.enbuild.2017.07.064.

Table 6

Architectures of backbone network.

Backbone	VGGNet16	MobileNetv2	Resnet18
N_{FN}/N_{FDN}	conv1	conv1	conv1
	conv2	bottleneck1-3	conv2_x
N_{BN}/N_{BDN}	conv3		conv3_x
	conv4	bottleneck4-13	conv4_x
	conv5		

A. APPENDIX

A.1. Network architectures and hyperparameters

Our detection network is described in Section 3. The VGGNet16, MobileNetv2, and Resnet18 backbone networks are applied for comparison. They are pre-trained on ImageNet (Russakovsky, Deng, Su, Krause, Satheesh, Ma, Huang, Karpathy, Khosla, Bernstein, Berg and Fei-Fei, 2015) dataset. Their detailed network architectures are shown in Table 6. The architecture of N_{FDN} is the same as N_{FN} 's, but the weights will be updated separately. If the resolution of the original image is $H \times W$, it will decrease to $H/4 \times W/4$ after N_{FN} and N_{FDN} . Similarly, the resolution will decrease to $H/16 \times W/16$ after N_{BN} and N_{BDN} . The entire model is trained by the SGD optimizer for 50 epochs. The learning rate is 10^{-2} and is decayed as 10^{-3} , 10^{-4} and 10^{-5} after 15, 35 and 42 epochs separately. The detector network contains 5 convolutional layers, which are initialized with standard normal distribution with 0.01 standard deviation. MPSN is also tested on DETR. We select the Resnet18 as the backbone network, then add a pseudo-siamese network and DFA to compare to the detection performance. The model is trained for 300 epochs. The learning rate of the backbone network is set to 10^{-5} and is decayed as 10^{-6} and 10^{-7} after 100 and 200 epochs separately. The batchsize is set to 1.

A.2. Gradient backpropagation

The derivatives of DFA in Section 3 are related to the Hadamard product. We construct the diagonal matrix so that the following equation holds.

$$\mathbf{h}_{bn} \odot \sigma(\mathbf{h}_{bdn}) = \text{Diag}(\mathbf{h}_{bn})\sigma(\mathbf{h}_{bdn}).$$

Besides, the element-wise function differential is

$$d(\sigma(\mathbf{h}_{bdn})) = \sigma(\mathbf{h}_{bdn})' \odot d(\mathbf{h}_{bdn}).$$

According to Eq. (5), we can obtain

$$\begin{aligned} & \frac{\partial L(\theta, \mathbf{I}_f, \mathbf{y}_f)}{\partial \mathbf{h}_{bdn}} \\ &= \frac{\partial L(\theta, \mathbf{I}_f, \mathbf{y}_f)}{\partial \mathbf{h}_{agg}} \cdot \frac{\partial \mathbf{h}_{agg}}{\partial \sigma(\mathbf{h}_{bdn})} \cdot \frac{\partial \sigma(\mathbf{h}_{bdn})}{\partial \mathbf{h}_{bdn}} \\ &= \frac{\partial L(\theta, \mathbf{I}_f, \mathbf{y}_f)}{\partial \mathbf{h}_{agg}} \cdot [\alpha \cdot \text{Diag}(\mathbf{h}_{bn}) + \beta \cdot \mathbf{I}] \\ & \quad \cdot \text{Diag}[\sigma(\mathbf{h}_{bdn}) \odot (1 - \sigma(\mathbf{h}_{bdn}))], \end{aligned} \quad (14)$$

where \mathbf{I} is the identity matrix, and $\mathbf{1}$ is the all-ones matrix.

A.3. The mathematical solution of small ϵ

According to the Eq. (1) and Eq. (10), we have

$$\begin{aligned} \mathbf{I}_{df}^a &= |\mathbf{I}_f^a - \mathbf{I}_{f-1}^a| \\ &= |\mathbf{I}_f - \mathbf{I}_{f-1} + \epsilon[\text{sign}(\nabla_{\mathbf{I}_f} L(\theta, \mathbf{I}_f, \mathbf{y}_f)) \\ & \quad - \text{sign}(\nabla_{\mathbf{I}_{f-1}} L(\theta, \mathbf{I}_{f-1}, \mathbf{y}_{f-1}))]|, \end{aligned}$$

thus,

$$\begin{aligned} \mathbf{I}_{df}^a - \mathbf{I}_{df} &\leq |\mathbf{I}_f - \mathbf{I}_{f-1}| + \epsilon|\text{sign}(\nabla_{\mathbf{I}_f} L(\theta, \mathbf{I}_f, \mathbf{y}_f)) \\ & \quad - \text{sign}(\nabla_{\mathbf{I}_{f-1}} L(\theta, \mathbf{I}_{f-1}, \mathbf{y}_{f-1}))| - |\mathbf{I}_f - \mathbf{I}_{f-1}| \\ &= \epsilon|\text{sign}(\nabla_{\mathbf{I}_f} L(\theta, \mathbf{I}_f, \mathbf{y}_f)) - \text{sign}(\nabla_{\mathbf{I}_{f-1}} L(\theta, \mathbf{I}_{f-1}, \mathbf{y}_{f-1}))|, \end{aligned}$$

$$\begin{aligned} \mathbf{I}_{df}^a - \mathbf{I}_{df} &\geq |\mathbf{I}_f - \mathbf{I}_{f-1}| - \epsilon|\text{sign}(\nabla_{\mathbf{I}_f} L(\theta, \mathbf{I}_f, \mathbf{y}_f)) \\ & \quad - \text{sign}(\nabla_{\mathbf{I}_{f-1}} L(\theta, \mathbf{I}_{f-1}, \mathbf{y}_{f-1}))| - |\mathbf{I}_f - \mathbf{I}_{f-1}| \\ &= -\epsilon|\text{sign}(\nabla_{\mathbf{I}_f} L(\theta, \mathbf{I}_f, \mathbf{y}_f)) - \text{sign}(\nabla_{\mathbf{I}_{f-1}} L(\theta, \mathbf{I}_{f-1}, \mathbf{y}_{f-1}))|. \end{aligned}$$

Let $t = |\text{sign}(\nabla_{\mathbf{I}_f} L(\theta, \mathbf{I}_f, \mathbf{y}_f)) - \text{sign}(\nabla_{\mathbf{I}_{f-1}} L(\theta, \mathbf{I}_{f-1}, \mathbf{y}_{f-1}))|$, thus,

$$-\epsilon t \geq \mathbf{I}_{df}^a - \mathbf{I}_{df} \leq \epsilon t. \quad (15)$$

Because ϵ is small in applications, we conduct Taylor expansion at \mathbf{I}_f :

$$\begin{aligned} g_\varphi(\mathbf{I}_f^a) - g_\varphi(\mathbf{I}_f) &= \frac{\partial g_\varphi(\mathbf{I}_f)}{\partial \mathbf{I}_f}^\top (\mathbf{I}_f^a - \mathbf{I}_f) + \frac{\partial^2 g_\varphi(\mathbf{I}_f)}{2\partial \mathbf{I}_f^2}^\top (\mathbf{I}_f^a \\ & \quad - \mathbf{I}_f)^2 + O(\epsilon^3) \approx \epsilon \frac{\partial g_\varphi(\mathbf{I}_f)}{\partial \mathbf{I}_f}^\top \text{sign}(\nabla_{\mathbf{I}_f} L(\theta, \mathbf{I}_f, \mathbf{y}_{f-1})) + \\ & \quad \frac{\epsilon^2}{2} \text{sign}^\top(\nabla_{\mathbf{I}_f} L(\theta, \mathbf{I}_f, \mathbf{y}_{f-1})) \frac{\partial^2 g_\varphi(\mathbf{I}_f)}{2\partial \mathbf{I}_f^2} \text{sign}(\nabla_{\mathbf{I}_f} L(\theta, \mathbf{I}_f, \mathbf{y}_{f-1})). \end{aligned}$$

Similarly, we conduct Multiple Taylor expansion at $\mathbf{I}_f, \mathbf{I}_{df}$:

$$\begin{aligned}
g_\theta(\mathbf{I}_f^a, \mathbf{I}_{df}^a) - g_\theta(\mathbf{I}_f, \mathbf{I}_{df}) &= \frac{\partial g_\theta(\mathbf{I}_f, \mathbf{I}_{df})^\top}{\partial \mathbf{I}_f} (\mathbf{I}_f^a - \mathbf{I}_f) + \\
&\frac{\partial g_\theta(\mathbf{I}_f, \mathbf{I}_{df})^\top}{\partial \mathbf{I}_{df}} (\mathbf{I}_{df}^a - \mathbf{I}_{df}) + \frac{1}{2} [(\mathbf{I}_f^a - \mathbf{I}_f)^\top (\mathbf{I}_{df}^a - \mathbf{I}_{df})^\top] \\
&\left[\begin{array}{cc} \frac{\partial^2 g_\theta(\mathbf{I}_f, \mathbf{I}_{df})}{\partial \mathbf{I}_f^2} & \frac{\partial^2 g_\theta(\mathbf{I}_f, \mathbf{I}_{df})}{\partial \mathbf{I}_f \partial \mathbf{I}_{df}} \\ \frac{\partial^2 g_\theta(\mathbf{I}_f, \mathbf{I}_{df})}{\partial \mathbf{I}_{df} \partial \mathbf{I}_f} & \frac{\partial^2 g_\theta(\mathbf{I}_f, \mathbf{I}_{df})}{\partial \mathbf{I}_{df}^2} \end{array} \right] \begin{bmatrix} (\mathbf{I}_f^a - \mathbf{I}_f) \\ (\mathbf{I}_{df}^a - \mathbf{I}_{df}) \end{bmatrix} + O(\epsilon^3) \\
&\leq \epsilon \frac{\partial g_\theta(\mathbf{I}_f, \mathbf{I}_{df})^\top}{\partial \mathbf{I}_f} \text{sign}(\nabla_{\mathbf{I}_f} L(\theta, \mathbf{I}_f, y_f)) + \epsilon \left| \frac{\partial g_\theta(\mathbf{I}_f, \mathbf{I}_{df})^\top}{\partial \mathbf{I}_{df}} \right| \\
&t + \frac{\epsilon^2}{2} \text{sign}^\top(\nabla_{\mathbf{I}_f} L(\theta, \mathbf{I}_f, y_f)) \frac{\partial^2 g_\theta(\mathbf{I}_f, \mathbf{I}_{df})}{\partial \mathbf{I}_f^2} \text{sign}(\nabla_{\mathbf{I}_f} L(\theta, \\
&\mathbf{I}_f, y_f)) + \epsilon^2 |\text{sign}^\top(\nabla_{\mathbf{I}_f} L(\theta, \mathbf{I}_f, y_f)) \frac{\partial^2 g_\theta(\mathbf{I}_f, \mathbf{I}_{df})}{\partial \mathbf{I}_f \partial \mathbf{I}_{df}}| t \\
&+ \frac{\epsilon^2}{2} t^\top \frac{\partial^2 g_\theta(\mathbf{I}_f, \mathbf{I}_{df})}{\partial \mathbf{I}_{df}^2} t.
\end{aligned}$$

When $\mathbf{NI_MPSN} \leq \mathbf{NI_FCHD}$:

$$\begin{aligned}
&\left\| \frac{1}{NC} \sum_{f=1}^N [g_\theta(\mathbf{I}_f^a, \mathbf{I}_{df}^a) - g_\theta(\mathbf{I}_f, \mathbf{I}_{df})] \right\|_2 \\
&\leq \left\| \frac{1}{(N+1)D} \sum_{f=0}^N [g_\varphi(\mathbf{I}_f^a) - g_\varphi(\mathbf{I}_f)] \right\|_2. \quad (16)
\end{aligned}$$

Both sides are quadratic functions of ϵ , thus,

$$|j\epsilon + \epsilon^2 k| \leq |l\epsilon + \epsilon^2 m| \Rightarrow |j + \epsilon k| \leq |l + \epsilon m|. \quad (17)$$

The small ϵ can be obtained mathematically.